

# Uniqueness range optimization of photocarrier transport parameter measurements using combined quantitative heterodyne lock-in carrierography imaging and photocarrier radiometry <sup>EP</sup>

Cite as: J. Appl. Phys. 125, 065701 (2019); <https://doi.org/10.1063/1.5083168>

Submitted: 28 November 2018 . Accepted: 22 January 2019 . Published Online: 12 February 2019

Peng Song, Alexander Melnikov,  Qiming Sun,  Andreas Mandelis, and  Junyan Liu

## COLLECTIONS

 This paper was selected as an Editor's Pick



View Online



Export Citation



CrossMark

## ARTICLES YOU MAY BE INTERESTED IN

[Jitter mitigation in low density discharge plasma cells for wakefield accelerators](#)

Journal of Applied Physics **125**, 063301 (2019); <https://doi.org/10.1063/1.5068753>

[Radiation-induced micro-structures as ground states of a Swift-Hohenberg energy functional](#)

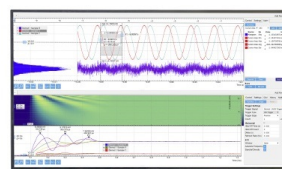
Journal of Applied Physics **125**, 065103 (2019); <https://doi.org/10.1063/1.5072798>

[Invited Article: Emerging soft bioelectronics for cardiac health diagnosis and treatment](#)

APL Materials **7**, 031301 (2019); <https://doi.org/10.1063/1.5060270>

Challenge us.

What are your needs for  
periodic signal detection?



Zurich  
Instruments



# Uniqueness range optimization of photocarrier transport parameter measurements using combined quantitative heterodyne lock-in carrierography imaging and photocarrier radiometry

Cite as: J. Appl. Phys. 125, 065701 (2019); doi: 10.1063/1.5083168

Submitted: 28 November 2018 · Accepted: 22 January 2019 ·

Published Online: 12 February 2019



Peng Song,<sup>1,2</sup> Alexander Melnikov,<sup>1</sup> Qiming Sun,<sup>1,3</sup>  Andreas Mandelis,<sup>1,3,a)</sup>  and Junyan Liu<sup>2,b)</sup> 

## AFFILIATIONS

<sup>1</sup>Center for Advanced Diffusion-Wave and Photoacoustic Technologies (CADIPT), University of Toronto, Toronto M5S 3G8, Canada

<sup>2</sup>School of Mechatronics Engineering, Harbin Institute of Technology, Harbin 150001, China

<sup>3</sup>Optoelectronic Information, University of Electronic Science and Technology of China, Chengdu 610054, China

<sup>a)</sup>Author to whom correspondence should be addressed: [mandelis@mie.utoronto.ca](mailto:mandelis@mie.utoronto.ca)

<sup>b)</sup>[jywlj@hit.edu.cn](mailto:jywlj@hit.edu.cn)

## ABSTRACT

Simulations were carried out to study the uniqueness range of Heterodyne Lock-in Carrierography (HeLIC) imaging measurements of carrier transport parameters (bulk lifetime, diffusion coefficient, and front and back surface recombination velocities) of silicon wafers. Theoretically, HeLIC can resolve all four transport parameters; however, in practice, the presence of experimental noise does not allow all those parameters to be measured reliably and uniquely from HeLIC images alone. An extended range of simultaneously determined unique transport parameters was attained through the combination of HeLIC camera pixel and photocarrier radiometry (PCR) experimental frequency response data via a multi-parameter fitting procedure. Two *n*- and *p*-type wafers with different surface recombination velocities were used to illustrate the simulation results. Quantitative HeLIC images of diffusion coefficients and surface recombination velocities were obtained, with bulk lifetime values determined from PCR frequency scan measurements. The combined approach was shown to be able to resolve all four transport parameters uniquely and thus reliably.

Published under license by AIP Publishing. <https://doi.org/10.1063/1.5083168>

## I. INTRODUCTION

The accurate determination of minority carrier transport parameters (i.e., carrier lifetime, diffusion coefficient, and surface recombination velocities) in silicon is important for process control and device modeling in the semiconductor and more specifically the photovoltaic industry. Photocarrier radiometry (PCR),<sup>1</sup> a spectrally gated frequency-domain photoluminescence (PL) modality that filters out thermal infrared photon emissions, employs a single-element near-infrared detector to evaluate photoexcited free-carrier density wave

(CDW) radiative recombination in electronic solids such as silicon wafers by recording the amplitude and phase of PL photon generated PCR signals. PCR can be used for the non-contact simultaneous determination of the transport parameters of silicon substrates<sup>2-4</sup> and devices<sup>5-7</sup> through best-fitting the amplitude- and phase-frequency dependencies to appropriate CDW theoretical models by means of suitable multi-parameter fitting processes.

High detection efficiency camera-based luminescence techniques like electroluminescence<sup>8</sup> and PL<sup>9</sup> are used to

characterize the performance of silicon materials and devices in the time domain.<sup>10-12</sup> Lock-in carrierography (LIC)<sup>13</sup> is an imaging counterpart of PCR. It is a contactless and calibration-free frequency domain PL imaging methodology that can yield quantitative effective lifetime images<sup>13-16</sup> and electrical parameters of solar cells.<sup>17,18</sup> To obtain quantitative images, heterodyne lock-in carrierography (HeLIC) was introduced to address the need for high frequency responses required to measure recombination lifetimes and other fast photocarrier relaxation processes, so as to overcome the limited frame rate of state-of-the-art near-infrared cameras. The heterodyne technique operates by employing two different modulation laser frequencies and has been successfully used to characterize the performance of silicon substrates.<sup>19,20</sup> It is worth mentioning that the heterodyne amplitude is the only effective signal channel for HeLIC because the heterodyne phase across all frequencies is close to 0° due to the small difference between the two superposed modulation frequencies. As a result, the simultaneous determination of carrier transport parameters using HeLIC amplitude only has not been investigated to-date. Recently, the bulk lifetime and the surface recombination velocity images of wet-cleaned silicon wafers were simultaneously obtained by best-fitting the HeLIC amplitude-frequency dependences to CDW theory under the assumptions of the known diffusion coefficient and fixed bulk lifetime, while surface processing (chemical clean) conditions were varied.<sup>21</sup>

In this paper, the suitability of HeLIC imaging for the quantitative determination of carrier transport parameters is examined. The uniqueness and ensuing reliability ranges for simultaneous determination of the carrier transport parameters were investigated by means of simulations which led to expanding those ranges through the combination of HeLIC and PCR measurements. The combined measurements were then used to construct quantitative images of Si wafer transport properties of two wafers (n- and p-type) with different surface recombination velocities.

## II. THEORY

PCR and its imaging counterpart, LIC, are frequency domain (FD) dynamic PL techniques, the signals of which are determined by the radiative recombination kinetics of excess carrier density waves generated by modulated laser beams. Under low injection conditions (meaning that the excess carrier density is much smaller than the doping density), the depth-dependent carrier distribution in a semiconductor wafer can be described by the one-dimensional carrier diffusion equation<sup>15,22,23</sup>

$$D \frac{\partial^2 \Delta n(t, z)}{\partial z^2} - \frac{\Delta n(t, z)}{\tau_b} - \frac{\partial \Delta n(t, z)}{\partial t} = -G_0 \beta e^{-\beta z} g(t), \quad (1)$$

where  $D$  is the minority carrier diffusion coefficient,  $\Delta n(t, z)$  is the photogenerated excess carrier density,  $\tau_b$  is the bulk lifetime,  $G_0$  is the average optical generation rate,  $\beta$  is the optical

absorption coefficient, and  $g(t)$  is the temporal modulation function.

The solution  $n(\omega, z)$  of the Fourier transform of Eq. (1) can be expressed as

$$\Delta n(\omega, z) = C_1 e^{-\sigma z} + C_2 e^{-\sigma(L-z)} - \frac{G_0 \beta}{D(\beta^2 - \sigma^2)} e^{-\beta z}, \quad (2)$$

where  $\sigma = [(\tau_b^{-1} + i\omega)/D]^{1/2}$  is the carrier density wavenumber,  $L$  is the wafer thickness,  $C_1$  and  $C_2$  are integration constants determined by the appropriate boundary conditions at the front and rear surfaces of the wafer,  $\omega = 2\pi f$  is the angular frequency, and  $f$  is the modulation frequency

$$\begin{aligned} D \left. \frac{d\Delta n(\omega, z)}{dz} \right|_{z=0} &= S_f \Delta n(\omega, z = 0), \\ D \left. \frac{d\Delta n(\omega, z)}{dz} \right|_{z=L} &= -S_r \Delta n(\omega, z = L), \end{aligned} \quad (3)$$

where  $S_f$  ( $S_r$ ) is the front (rear) surface recombination velocity (SRV).

### A. Homodyne photocarrier radiometry (HoPCR)

The conventional linearized PCR response represents the homodyne model which can be expressed in the form<sup>22</sup>

$$S_{Ho}(\omega) = C \int_0^L \Delta n(\omega, z) dz, \quad (4)$$

where  $C$  is a proportionality factor that takes into account the band-to-band carrier radiative quantum efficiency and the frequency-dependent properties of the instrumentation.<sup>1,16</sup>

### B. Heterodyne photocarrier radiometry (HePCR)

The linearized heterodyne model can be expressed as<sup>15</sup>

$$S_{He}(\Delta\omega) = C' \int_0^L \Delta n(-\omega_1, z) \Delta n(\omega_2, z) dz, \quad (5)$$

where  $\Delta\omega = |\omega_2 - \omega_1|$  and  $C'$  is a proportionality factor. Here,  $\Delta n(-\omega_1, z) = \Delta n^*(\omega_1, z)$  indicates the nonlinear frequency mixing and the beat-frequency detection nature of heterodyne signals, where  $*$  denotes complex conjugation.

## III. NUMERICAL SIMULATIONS OF HOPCR AND HEPER THEORY AND RESULTS

To determine the transport parameters of Si wafers, both the experimental amplitude and phase of HoPCR can be recorded and then fitted to Eq. (4) using a multi-parameter fitting.<sup>1,6</sup> In our previous study,<sup>24</sup> the ability of PCR for the

accurate determination of carrier lifetime was estimated to encompass values as long as 100 ms. If the diffusion coefficient is known, the carrier lifetime and front surface recombination velocity can be determined with uncertainties approximately  $\pm 20\%$  or less. However, for HeLIC, the difference between the two beating modulation frequencies is always small (2 Hz in our case), so the heterodyne phase is nearly  $0^\circ$  as mentioned above. Therefore, only heterodyne amplitude-frequency dependencies were fitted to Eq. (5) via a multi-parameter fitting procedure.<sup>21</sup> In this section, the sensitivity of HeLIC to determine transport parameters (bulk lifetime,  $\tau_b$ ; diffusion coefficient,  $D$ ; front surface recombination velocity,  $S_f$ ; and rear surface recombination velocity,  $S_r$ ) uniquely, and thus reliably, is investigated using a numerical simulation method.

In the numerical simulations, the absorption coefficient of the wafer,  $\beta$ , was assumed to be  $789 \text{ cm}^{-1}$ , which corresponds to crystalline silicon irradiated with  $808 \text{ nm}$ <sup>25</sup> light. The wafer thickness,  $L$ , was measured to be  $690 \mu\text{m}$ . The heterodyne amplitude at various frequencies was calculated through Eq. (5) with transport parameter values assumed to be  $\tau_b = 1 \text{ ms}$ ,  $D = 18 \text{ cm}^2/\text{s}$ ,  $S_f = 10 \text{ cm/s}$ , and  $S_r = 50 \text{ cm/s}$ . When the effect of an individual transport parameter on the heterodyne amplitude was investigated, the other transport parameters remained fixed at their assumed values.

The influence of transport parameters on the heterodyne amplitude at various frequencies is shown in Fig. 1. From Fig. 1(a), it is found that at 100 Hz, the amplitude increases with increasing carrier lifetime and becomes saturated above  $\tau_b = 10 \text{ ms}$ . This behavior is similar to that described previously.<sup>24</sup> The bulk lifetime has a weak influence on the heterodyne amplitude at high frequencies ( $\omega = 2\pi f \gg \tau_b^{-1}$ ). This is so because the PL signal is always proportional to the diffusion length which takes on the form  $L_{ac} \approx (D^*/\omega)^{1/2}$  at high frequencies, independent of bulk lifetime. In that frequency range, the carrier diffusion wave behaves entirely like a thermal wave. It follows that to accurately measure a long bulk lifetime, the heterodyne amplitude should be measured at low frequencies. Figure 1(b) shows that the diffusion coefficient affects the heterodyne amplitude at all frequencies: increasing  $D$  moves the centroid of the CDW deeper into the wafer bulk, thereby decreasing the carrier density and the heterodyne signal. Figure 1(c) shows the amplitude as a function of the front surface recombination velocity at 0.1 kHz, 1 kHz, and 10 kHz. The heterodyne amplitude is sensitive to the front surface recombination velocity in the range of 0.1–100 m/s. In this range, the amplitude decreases with increasing surface recombination velocity, which means that the surface recombination velocity can be accurately determined. Figure 1(d) shows the amplitude dependence on the rear

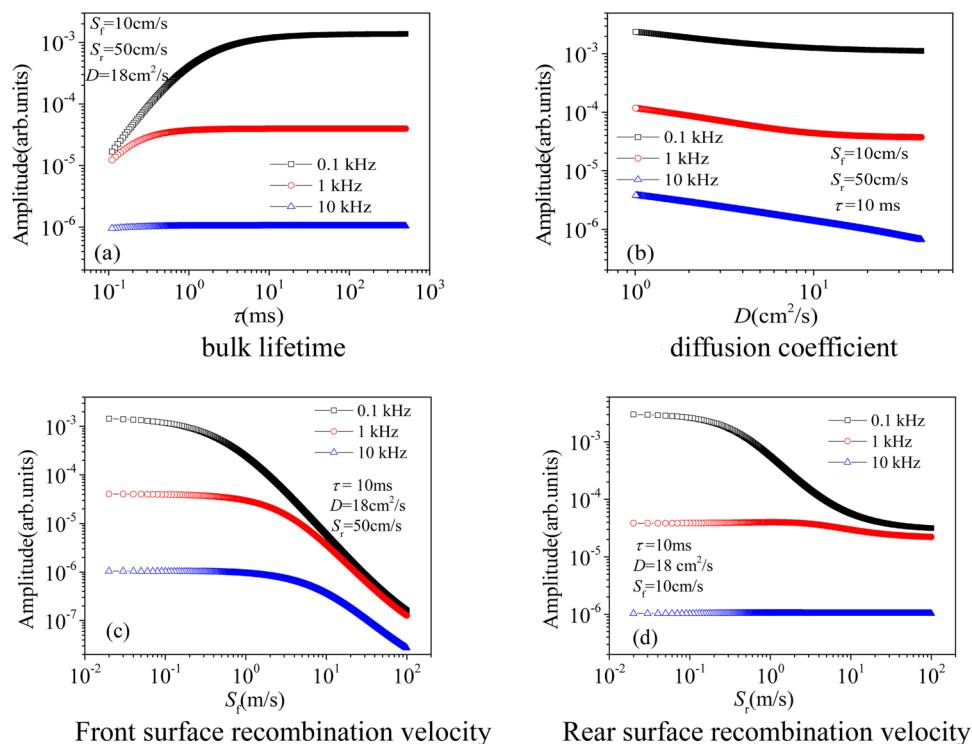


**FIG. 1.** Simulated heterodyne PCR amplitude as a function of transport parameters. The values assumed for  $\tau_b$ ,  $D$ ,  $S_f$ , and  $S_r$  are 10 ms,  $18 \text{ cm}^2/\text{s}$ ,  $10 \text{ cm/s}$ , and  $50 \text{ cm/s}$ , respectively. (a) Bulk lifetime, (b) diffusion coefficient, (c) front surface recombination velocity, and (d) rear surface recombination velocity.

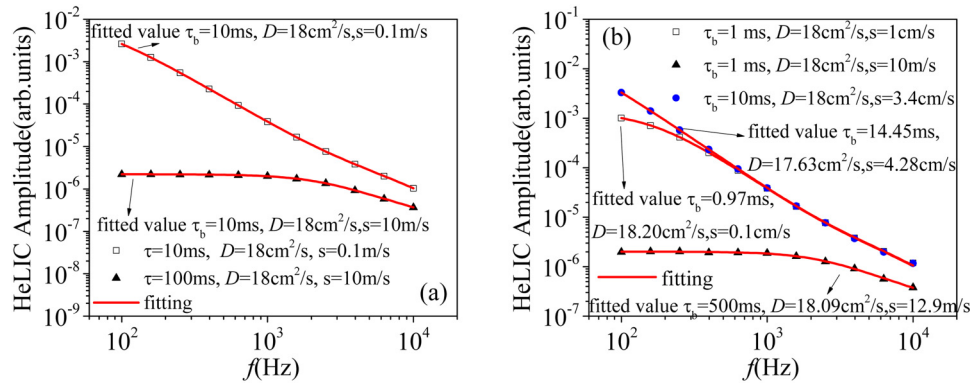


**FIG. 2.** Simulated HeLIC amplitude dependence on frequency and corresponding best-fitted dependencies and results. (a) Amplitude-frequency dependence according to Eq. (5) and (b) amplitude-frequency dependence with 10% added random noise.

surface recombination velocity at 0.1kHz, 1kHz, and 10 kHz. Similar to conventional HoPCR,<sup>24</sup> HeLIC is not sensitive enough to accurately determine high rear surface recombination velocities or at high frequencies where the ac carrier diffusion length is much shorter than the thickness of the wafer.

The foregoing simulation results show that the HeLIC methodology can be used to determine the four transport parameters simultaneously theoretically via multi-parameter fitting within specific value ranges. Reducing the unknown parameters by one or more can highly improve the accuracy of fitting results. To test this feature, the front and rear surface recombination velocity were assumed to be the same in a recent study,<sup>21</sup> i.e.,  $S_f = S_r \equiv s$ . In our best-fitting program, we used the `fminsearchbnd` solver<sup>26</sup> to minimize the sum of the squares of errors between the experimental and calculated data.<sup>5</sup> A simulation method was employed to explore the validity of the fitting program. The simulated HeLIC amplitude data with two sets of transport parameters and 11 points in the frequency range from 100 Hz to 10 kHz were calculated with known parameters and are shown in Fig. 2(a). The best-fitted parameters were also obtained and are shown in Fig. 2(a). They were found to be exactly the same as the assumed parameters in both cases.

The range of these parameters that can be accurately determined by HeLIC simulated data generated by Eq. (5) with experimental errors was identified. The simulated HeLIC amplitude data with 11 points were calculated with the values shown in Table I assuming  $D = 18 \text{ cm}^2/\text{s}$ . Worst-case random noise corresponding to average measurement errors on the order of 10% in view of the fact that the amplitude at the highest frequency fluctuates by  $\pm 10\%$  was added to each simulated datum. Figure 2(b) shows the two sets of simulated data and the corresponding best-fitted dependencies:  $D = 18 \text{ cm}^2/\text{s}$ ,  $\tau_b = 1 \text{ ms}$ , and  $s = 1 \text{ cm/s}$  for a low surface recombination velocity case (Case I);  $D = 18 \text{ cm}^2/\text{s}$ ,  $\tau_b = 1 \text{ ms}$ , and  $s = 10 \text{ m/s}$  for a high surface recombination velocity case (Case II); and  $D = 18 \text{ cm}^2/\text{s}$ ,  $\tau_b = 10 \text{ ms}$ , and  $s = 3.4 \text{ cm/s}$  for the case where

the bulk lifetime is equal to the surface recombination lifetime (Case III). For Case I, the best-fitted diffusion coefficient and bulk lifetime were close to the simulated values; however, the fitted SRV exhibited a large difference with the pre-set value. For Case II, the fitted diffusion coefficient and SRV were close to the simulated values; however, the fitted bulk lifetime was very different from the pre-set lifetime. For Case III; the three fitted parameters (bulk lifetime, diffusion coefficient, and SRV) were close to the simulated values. In all three cases, the diffusion coefficient could be resolved accurately with the fitted error for  $D$  being less than  $\pm 5.6\%$ . In this analysis, a given parameter was assumed to be resolved if the best-fit error for that parameter was less than  $\pm 30\%$ .

Table I shows the ability of HeLIC to resolve the transport parameters for various combinations of lifetime and surface recombination velocity values. The diffusion coefficient can always be resolved in all cases. Bulk lifetimes or SRVs can be resolved with added noise on the order of 10%.

**TABLE I.** The value ranges of HeLIC-determined bulk lifetimes and/or surface recombination velocities from calculated data with added random noise simulating experimental signal levels.

$\tau_b$ (ms) \ $s$ (m/s)		$\tau_b$ (ms)			
		0.1	1	10	100
34.03	0.01				
3.426	0.1				
0.366	1				
0.06	10				
0.029	100				

where

$\tau_b$ and $s$ unresolved	$\tau_b$ resolved	$s$ resolved
-----------------------------	-------------------	--------------

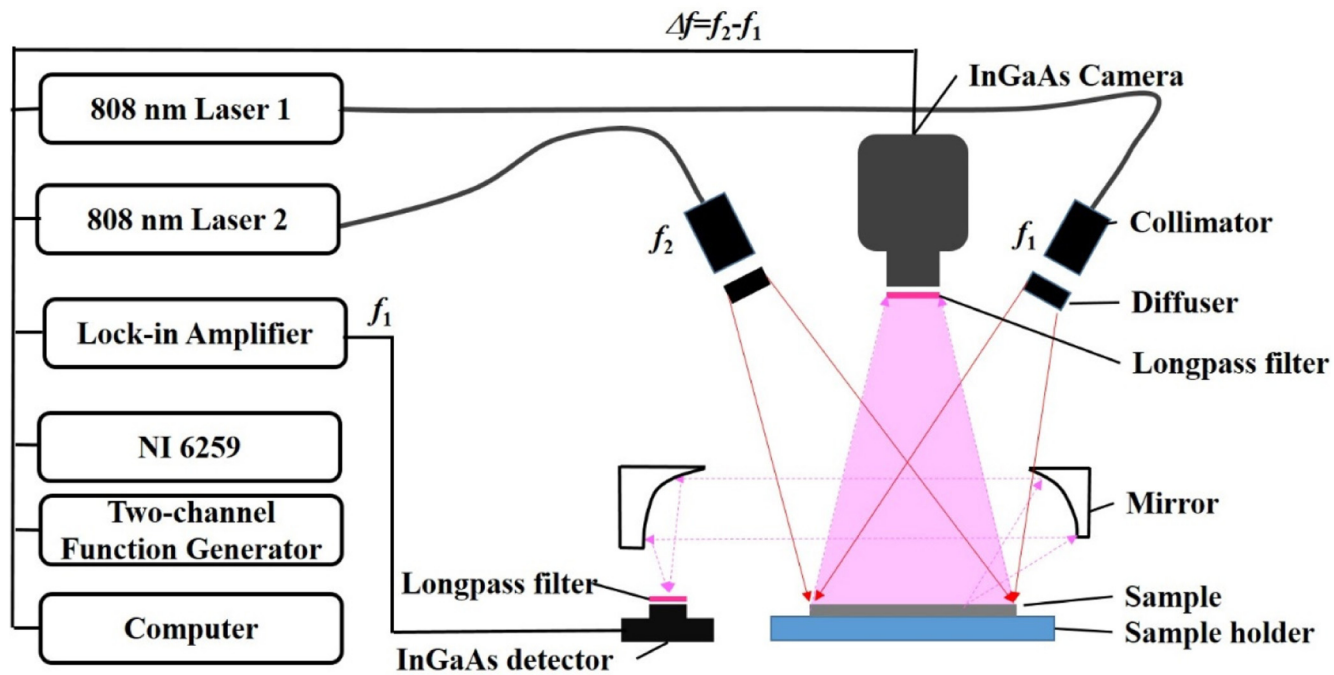


FIG. 3. A schematic of the combined experimental LIC and PCR system.

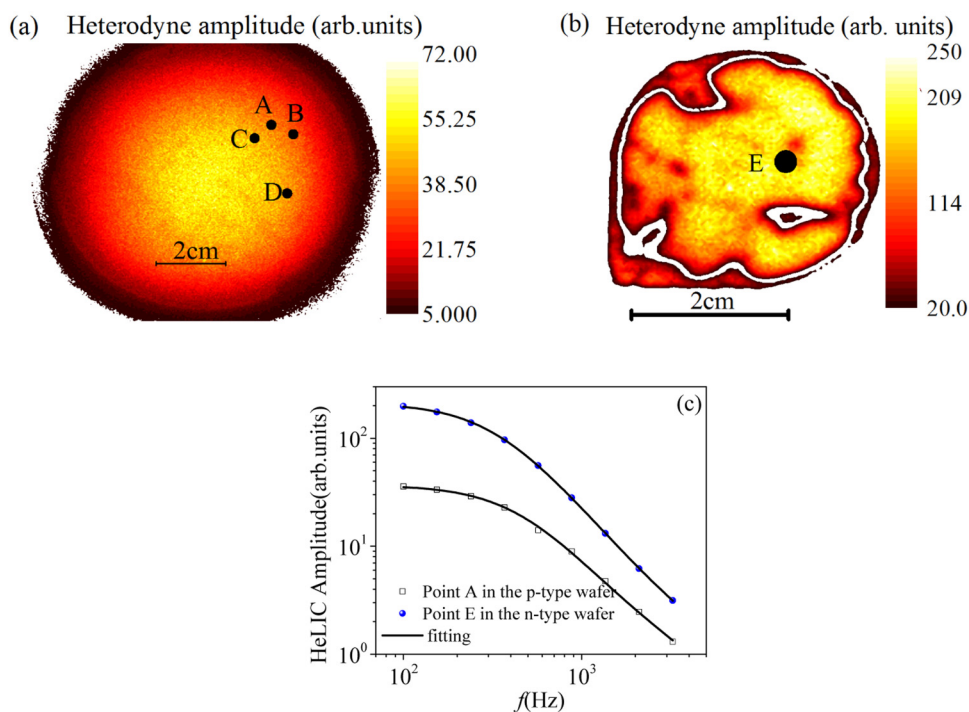


FIG. 4. Heterodyne amplitude image at  $f_1 = 100$  Hz for (a) the  $p$ -type wafer, (b) the  $n$ -type wafer, and (c) the HeLIC amplitude-frequency responses and best-fits to Eq. (5) at point A in (a) and point E in (b).

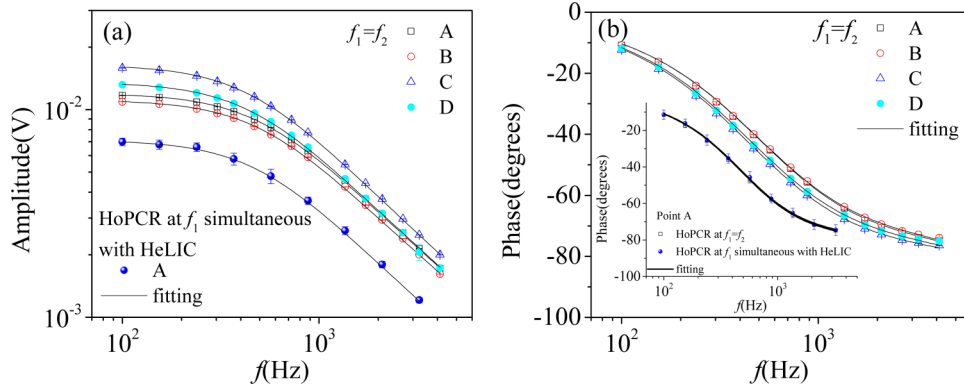


FIG. 5. HoPCR amplitude (a) and phase (b) at point A of the  $p$ -type wafer in Fig. 4(a) measured at  $f_1$  simultaneously with HeLIC. Also shown are data from points B, C, and D and their best-fits to Eq. (5).

Table I also shows the surface lifetime,  $\tau_s$ , a function of SRV.<sup>27</sup> If the bulk lifetime is much higher than the surface lifetime, the SRV can be resolved. On the other hand, if the bulk lifetime is much smaller than the surface lifetime, the former can be resolved. As an outcome of the foregoing simulations, it was found that the simultaneous improvement of the resolution range of bulk lifetime and SRV requires better matching frequency range, more frequency data, and better signal-to-noise ratio (SNR) performance of the experimental system. In addition, it was determined that conventional HoPCR can be used to improve the simultaneous and precise determination of the transport parameters.<sup>22</sup> Therefore, in the experimental plan for this work, combined HeLIC and HoPCR were used for reliable simultaneous resolution of the transport parameters.

#### IV. EXPERIMENTAL RESULTS AND DISCUSSION

A schematic diagram of the experimental HeLIC system combined with PCR is shown in Fig. 3. Two 45-W, 808-nm

fiber-coupled diode lasers were used to illuminate sample areas up to  $10 \times 10 \text{ cm}^2$ . These two lasers were sine-wave modulated with frequencies  $f_1$  and  $f_2 = f_1 + 2 \text{ Hz}$  using a two-channel function generator. The laser beams were collimated, homogenized, and spread by a microlens array across the area. The mean intensity of each laser was  $100 \text{ mW/cm}^2$ . An InGaAs camera (bandwidth: 900–1700 nm,  $320 \times 256$  pixels, exposure time: 0.13–16.6 ms) was used to measure HeLIC amplitude signals. A data acquisition card (NI USB-6259) was employed to generate the reference (2 Hz) and camera-trigger signals. For PCR, a single-element InGaAs detector was used to measure the signal amplitude and phase. The reflected laser beam was blocked with a 1000-nm longpass filter located in front of the camera and the InGaAs detector. The camera and the detector recorded signals at the same time. A lock-in amplifier demodulated the amplitude and phase of PCR signals. Synchronous oversampling<sup>28</sup> with external triggering of the camera was implemented for HeLIC imaging. Simultaneously with the HeLIC measurements, the

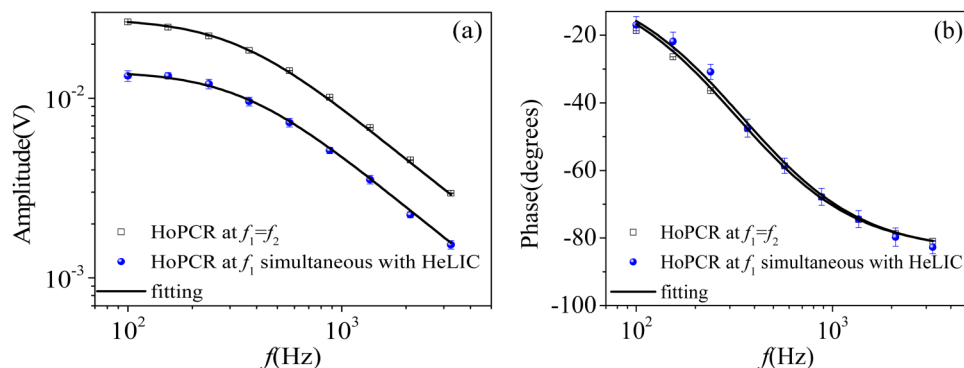


FIG. 6. HoPCR amplitude (a) and phase (b) at point E of the  $n$ -type wafer in Fig. 4(b) measured at  $f_1$  simultaneously with HeLIC.

**TABLE II.** Best-fitted HoPCR amplitude and phase transport parameters at point A for the  $p$ -type wafer and point E for the  $n$ -type wafer measured at  $f_1 = f_2$  and at  $f_1$  simultaneously with HeLIC measured at  $f_1, f_2 = f_1 + 2$  Hz.

Wafer type	Measurement method	$\tau_b$ (ms)	$D$ (cm <sup>2</sup> /s)	$s$ (m/s)
$p$ -type	HoPCR at $f_1 = f_2$	$1.46 \pm 0.05$	$10.4 \pm 0$	$0.91 \pm 0.01$
	HoPCR at $f_1$ simultaneous with HeLIC at $f_1, f_2 = f_1 + 2$ Hz	$1.04 \pm 0.02$	$9.4 \pm 0.02$	$0.81 \pm 0.02$
$n$ -type	HoPCR at $f_1 = f_2$	$1.48 \pm 0.01$	$2.83 \pm 0.01$	$0.23 \pm 0.01$
	HoPCR at $f_1$ simultaneous with HeLIC at $f_1, f_2 = f_1 + 2$ Hz	$1.30 \pm 0.18$	$2.44 \pm 0.03$	$0.19 \pm 0.02$

lock-in amplifier demodulated the PCR signals at frequency  $f_1$  or  $f_2$ .

Two samples were measured. Sample I was a 150-mm, 690- $\mu$ m thick silicon wafer ( $p$ -type, B-doped) with both surfaces passivated with oxide layers. Sample II was a 290- $\mu$ m thick  $n$ -type (P-doped) 100-mm silicon wafer with both surfaces partly passivated with amorphous-Si ( $\alpha$ -Si). Frequency scan experiments were performed on these two wafers.

Figures 4(a) and 4(b) are the HeLIC amplitude images of sample I and sample II at  $f_1 = 100$  Hz, respectively. HeLIC pixel amplitude-frequency dependencies at point A in Fig. 4(a) and point E in Fig. 4(b), as well as the corresponding best-fits to Eq. (5), are shown in Fig. 4(c). At the same time, HoPCR amplitudes and phases at  $f_1$  at Point A and Point E were also recorded. The selected points in Figs. 4(a) and 4(b) were used for conventional PCR experiments with  $f_1 = f_2$ .

Figure 5 shows the HoPCR amplitude-frequency and phase-frequency scans at point A performed at  $f_1$  simultaneously with HeLIC performed at  $f_1$  and  $f_2 = f_1 + 2$  Hz. The conventional PCR amplitudes and phases of points A, B, C, and D of sample I are also shown in Fig. 5. Similar data obtained at point E in Fig. 4 are shown in Fig. 6. The PCR amplitude obtained with the two laser beams and  $f_1 = f_2$  is higher than that measured with only one laser on at  $f_1$ , as expected, and the phases are essentially coincident, as expected in the signal linearized limit.

The best-fitted results (amplitude and phase) to Eq. (4) at points A and E obtained with two different measurements from HoPCR and simultaneously from HeLIC at  $f_1, f_2 = f_1 + 2$  Hz and with HoPCR frequency response data with  $f_1 = f_2$  are shown in Table II. The transport parameters of the  $p$ - and  $n$ -type wafers obtained with PCR at  $f_1$  simultaneously with HeLIC at  $f_1, f_2 = f_1 + 2$  Hz were found to be in good agreement with those obtained using PCR at  $f_1 = f_2$ . Note that the best-fitted value of the minority carrier diffusion coefficient of the  $n$ -type wafer was smaller than that of the  $p$ -type wafer as expected.<sup>23</sup> Based on the simulations, only two parameters

could be resolved using HeLIC alone. Both frequency range and parameter range, including reducing signal noise, are key factors determining how many parameters can be resolved. The use of PCR and the concomitant high SNR of its two channel signal (amplitude and phase) outputs simultaneously with the lower-SNR, single-channel (amplitude) pixel frequency dependence of HeLIC images, strengthened the uniqueness of the transport parameter measurements.<sup>24</sup> Specifically for these two samples, the surface recombination velocity and the diffusion coefficient could be uniquely resolved. In order to resolve three transport parameters, the best-fitted bulk lifetime from the HoPCR measurement was employed. For the multi-parameter best-fitting procedure of the HeLIC pixel frequency response, the PCR bulk lifetime was fixed and the diffusion coefficient and the surface recombination velocity were varied. Table III shows the best-fitted  $D$  and  $s$  once the bulk lifetime is fixed for points A and E of the two samples of Fig. 4, respectively. The best-fitted  $D$  and  $s$  values using HeLIC also coincide with, or are very close to, the values from the PCR measurements in Table II. This consistency of measurement results shows that HeLIC can precisely and uniquely (therefore, reliably) characterize the transport parameters like PCR does, despite the fact that there is only one signal channel available in the HeLIC pixel frequency response. This conclusion sets the stage for fast quantitative HeLIC imaging of transport properties of semiconductor materials and devices to replace the time-consuming and inefficient PCR raster scanning of wafer surfaces. Table IV shows the transport parameters obtained at points A, B, C, and D on sample I using conventional HoPCR measurements. The local bulk lifetimes are very close to each other and can be assumed to be approximately constant within standard deviation over the entire  $p$ -type Si wafer. Using this assumption, Fig. 7 shows the diffusion coefficient and SRV images for the two samples after the bulk lifetime was fixed, assumed to be constant. Compared to the minority

**TABLE III.** Best-fitted HeLIC amplitude transport parameters at point A of the  $p$ -type wafer and point E of the  $n$ -type wafer. The bulk lifetimes were obtained from HoPCR measurements.

Wafer type	$\tau_b$ (ms)	$D$ (cm <sup>2</sup> /s)	$s$ (m/s)
$p$ -type	1.46 (fixed)	10.65	0.81
$n$ -type	1.30 (fixed)	3.31	0.20

**TABLE IV.** Best-fitted transport parameters at four points of the  $p$ -type wafer in Fig. 4 from PCR measurements at  $f_1 = f_2$ .

$p$ -type wafer	$\tau_b$ (ms)	$D$ (cm <sup>2</sup> /s)	$s$ (m/s)
Point A	$1.46 \pm 0.05$	$10.4 \pm 0$	$0.91 \pm 0.01$
Point B	$1.45 \pm 0.22$	$8.38 \pm 0.35$	$1.01 \pm 0.05$
Point C	$2.13 \pm 1.06$	$10 \pm 0.18$	$0.87 \pm 0.11$
Point D	$1.25 \pm 0.25$	$8.85 \pm 0.25$	$0.80 \pm 0.07$

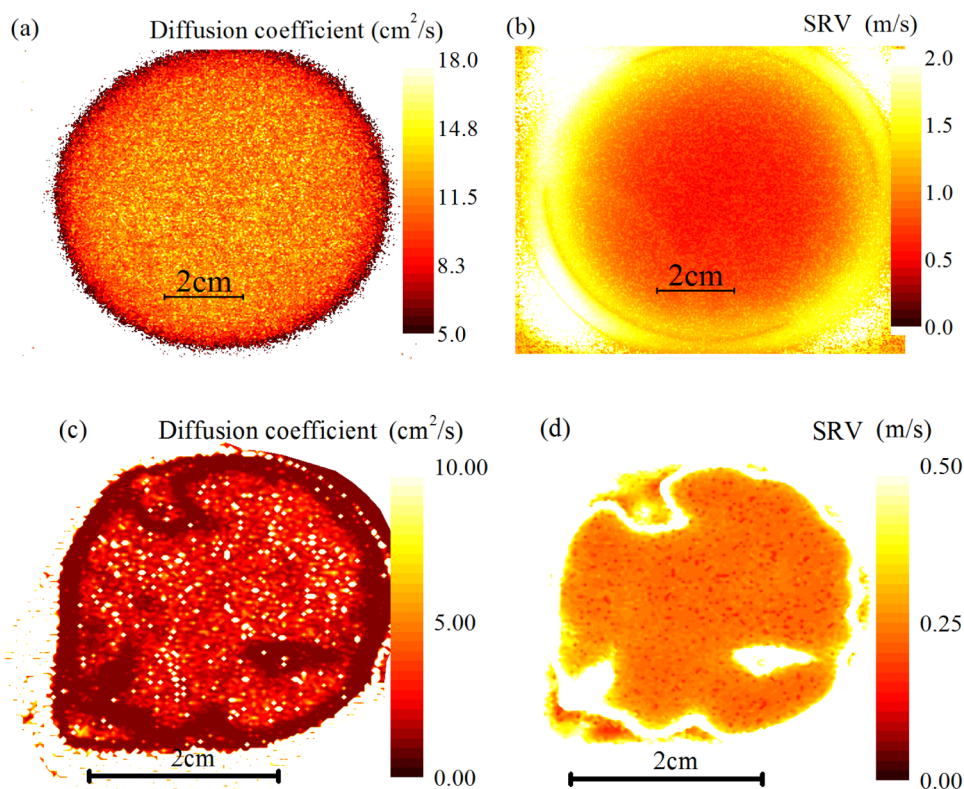


**FIG. 7.** Quantitative SRV and diffusion coefficient images of the *p*-type and the *n*-type wafers using HeLIC pixel amplitude responses. The spatially resolved bulk lifetime for each wafer was measured to be approximately constant as obtained from PCR measurements. (a) Diffusion coefficient image of the *p*-type wafer; (b) SRV image for the *p*-type wafer; (c) diffusion coefficient image for the *n*-type wafer; and (d) SRV image for the *n*-type wafer.

carrier (holes) diffusion coefficient image of the *n*-type wafer, the mean value of the minority carrier (electrons) diffusion coefficient of the *p*-type wafer shown in Figs. 7(a) and 7(c), respectively, is higher, as expected. The mean value of the SRV of the *n*-type wafer was found to be smaller than the *p*-type wafer as shown in Figs. 7(b) and 7(d). It can thus be concluded that the amorphous-Si layer has a better surface quality than the oxide layer.

## V. CONCLUSIONS

In this work, simulations and experimental validations were carried out to investigate and optimize the uniqueness and reliability ranges of carrier transport parameter measurements (bulk lifetime, diffusion coefficient, and surface recombination velocities) of *n*- and *p*-type silicon wafers, using multi-parameter best-fits of HeLIC image pixel frequency responses to heterodyne theory to fit experimental data in the presence of noise. The simulations produced value ranges in which transport parameters can be measured uniquely, thus yielding quantitative HeLIC images of those parameters. HeLIC was found to be able to resolve the diffusion coefficient and bulk lifetime *and/or* surface recombination velocity

depending on the relative values of the latter two quantities. It was found that combined simultaneous HeLIC and HoPCR measurements were effective and sufficient for uniquely resolving all four transport parameters, thereby yielding quantitative images of the diffusion coefficient and SRV of two silicon samples, *n*- and *p*-type wafers with different surface recombination velocities and similar bulk lifetimes.

## ACKNOWLEDGMENTS

A.M. is grateful to the Natural Sciences and Engineering Research Council of Canada (NSERC) for a Discovery grant, to the Canada Research Chairs Program, and to the Chinese Recruitment Program of Global Experts (Thousand Talents). J.L. and P.S. acknowledge the National Natural Science Foundation of China (NNSFC) (Grant No. 61571153). P.S. also gratefully acknowledges the financial support from the China Scholarship Council.

## REFERENCES

- <sup>1</sup>A. Mandelis, J. Batista, and D. Shaughnessy, *Phys. Rev. B* **67**, 205208 (2003).
- <sup>2</sup>J. Batista, A. Mandelis, and D. Shaughnessy, *Appl. Phys. Lett.* **82**, 4077 (2003).

- <sup>3</sup>B. Li, D. Shaughnessy, A. Mandelis, J. Batista, and J. Garcia, *J. Appl. Phys.* **96**, 186 (2004).
- <sup>4</sup>J. Liu, P. Song, L. Qin, F. Wang, and Y. Wang, *Acta Phys. Sin.* **64**, 087804 (2015).
- <sup>5</sup>Y. Zhang, A. Melnikov, A. Mandelis, B. Halliop, N. P. Kherani, and R. Zhu, *Rev. Sci. Instrum.* **86**, 033901 (2015).
- <sup>6</sup>P. Song, J. Y. Liu, H. M. Yuan, M. Oliullah, F. Wang, and Y. Wang, *Nucl. Instrum. Methods Phys. Res. B* **383**, 171 (2016).
- <sup>7</sup>L. Hu, M. Liu, A. Mandelis, Q. Sun, A. Melnikov, and E. H. Sargent, *Sol. Energy Mater. Sol. Cells* **174**, 405 (2018).
- <sup>8</sup>T. Fuyuki, H. Kondo, T. Yamazaki, Y. Takahashi, and Y. Uraoka, *Appl. Phys. Lett.* **86**, 262108 (2005).
- <sup>9</sup>T. Trupke, R. A. Bardos, M. C. Schubert, and W. Warta, *Appl. Phys. Lett.* **89**, 044107 (2006).
- <sup>10</sup>P. Würfel, T. Trupke, T. Puzzer, E. Schäffer, W. Warta, and S. W. Glunz, *J. Appl. Phys.* **101**, 123110 (2007).
- <sup>11</sup>S. Herlufsen, J. Schmidt, D. Hinken, K. Bothe, and R. Brendel, *Phys. Status Solidi Rapid Res. Lett.* **2**, 245 (2008).
- <sup>12</sup>J. A. Giesecke, M. Kasemann, and W. Warta, *J. Appl. Phys.* **106**, 014907 (2009).
- <sup>13</sup>A. Melnikov, A. Mandelis, J. Tolev, P. Chen, and S. Huq, *J. Appl. Phys.* **107**, 114513 (2010).
- <sup>14</sup>Q. M. Sun, A. Melnikov, and A. Mandelis, *Appl. Phys. Lett.* **101**, 242107 (2012).
- <sup>15</sup>Q. Sun, A. Melnikov, and A. Mandelis, *Phys. Status Solidi A* **213**(2), 405–411 (2016).
- <sup>16</sup>P. Song, A. Melnikov, Q. Sun, A. Mandelis, and J. Liu, *Semicond. Sci. Technol.* **33**, 12LT01 (2018).
- <sup>17</sup>A. Mandelis, Y. Zhang, and A. Melnikov, *J. Appl. Phys.* **112**, 054505 (2012).
- <sup>18</sup>P. Song, J. Liu, M. Oliullah, and Y. Wang, *Phys. Status Solidi Rapid Res. Lett.* **11**(7), 1700153 (2017).
- <sup>19</sup>A. Melnikov, P. Chen, Y. Zhang, and A. Mandelis, *Int. J. Thermophys.* **33**, 2095 (2012).
- <sup>20</sup>Q. M. Sun, A. Melnikov, and A. Mandelis, *Int. J. Thermophys.* **36**, 1274 (2015).
- <sup>21</sup>Q. Sun, A. Melnikov, A. Mandelis, and R. H. Pagliaro, *Appl. Phys. Lett.* **112**, 012105 (2018).
- <sup>22</sup>A. Mandelis, *Diffusion-Wave Fields Mathematical Methods and Green Functions* (Springer, New York, 2001), p. 586.
- <sup>23</sup>J. A. Giesecke, M. Kasemann, M. C. Schubert, P. Würfel, and W. Warta, *Prog. Photovolt Res. Appl.* **18**, 10–19 (2010).
- <sup>24</sup>B. Li, D. Shaughnessy, and A. Mandelis, *J. Appl. Phys.* **97**, 023701 (2005).
- <sup>25</sup>M. A. Green and M. J. Keevers, *Prog. Photovoltaics Res. Appl.* **3**, 189 (1995).
- <sup>26</sup>J. D'Errico, see <http://www.mathworks.com/matlabcentral/fileexchange/8277> for fminsearchbnd code.
- <sup>27</sup>See <https://www.pveducation.org/pvc/drom/characterisation/surface-recombination> for surface recombination.
- <sup>28</sup>O. Breitenstein, W. Warta, and M. Langenkamp, *Lock-in Thermography* (Springer, Berlin, 2010), p. 18.